RSC Advances

PAPER

View Article Online
View Journal | View Issue

Cite this: *RSC Adv.*, 2025, **15**, 45333

A covalent organic framework/reduced graphene oxide composites-based electrochemical sensing platform for the detection of enrofloxacin

Pian Wu,†[a] Jun Liu,†[b] Siyu Lu,[c] Anlin zhang,[ef] Yuan Tian,[a] Jun Xiang,[d] Shanlin Wang[c] and Ping Ding *[a]

The accurate, sensitive, and efficient detection of enrofloxacin (ENR) residues is critically important for protecting public health and ensuring environmental safety. Herein, a novel electrochemical sensing platform based on a TAPB–PDA covalent organic framework integrated with reduced graphene oxide (TAPB–PDA-COFs/RGO) for the sensitive and selective detection of ENR in aqueous environments was developed. The TAPB–PDA-COFs/RGO leverages the high surface area and ordered pore structure of COFs alongside the excellent electrical conductivity of RGO, resulting in enhanced electrochemical performance. Under optimized conditions, the sensor exhibited a wide linear detection range (0.01–150 μmol L^{-1}), a low detection limit (0.028 μmol L^{-1}), and high selectivity even in the presence of structurally similar fluoroquinolones. The sensor also demonstrated good stability and reproducibility. When applied to spiked tap water samples, the platform achieved satisfactory recoveries of 84.1–99.7% and outperformed the conventional HPLC method at low ENR concentrations. These results highlighted the potential of the TAPB–PDA-COFs/RGO composite as a promising tool for environmental monitoring of antibiotic residues.

Received 10th October 2025
Accepted 11th November 2025

DOI: 10.1039/d5ra07733h

rsc.li/rsc-advances

1 Introduction

The extensive and indiscriminate use of antibiotics has become a significant global public health concern that demands urgent attention.[1] Antibiotics, comprising natural, semi-synthetic, and synthetic compounds, are widely employed to prevent and treat infectious diseases in both human and veterinary medicine, as well as in livestock farming to promote growth and enhance productivity.[2,3] However, a substantial fraction of administered antibiotics is not fully metabolized and is excreted in unmetabolized or partially metabolized forms. These residues can persist in environmental matrices, bioaccumulate through the food chain, and ultimately present significant health hazards to humans and animals.[4,5] Among various classes of antibiotics, fluoroquinolones are particularly prominent due to their broad-spectrum antimicrobial activity and mechanism of action, which involves the inhibition of bacterial DNA synthesis.[6] Enrofloxacin (ENR), a third-generation fluoroquinolone, is one of the most commonly used veterinary drugs for disease management in livestock.[7] However, its widespread application has led to the accumulation of residues in animal tissues and aquatic environments, posing ecological and public health hazards.[8,9] To mitigate these risks, the Chinese Ministry of Agriculture sets the maximum residue limits for ENR and its metabolite ciprofloxacin at 100 μg kg^{-1} in animal muscle and fat.[10] While the United States Food and Drug Administration has banned the use of ENR in certain livestock and poultry.[11] Consequently, the development of accurate, sensitive, and efficient detection methods for ENR residues in environmental samples is of paramount importance for safeguarding public health and environmental integrity.

Conventional analytical techniques for the detection of ENR residues in environmental and food matrices include high-performance liquid chromatography (HPLC),[12] gas chromatography-mass spectrometry (GC-MS),[13] liquid chromatography-mass spectrometry (LC-MS),[14] and capillary electrophoresis.[15] While these methods offer high accuracy and sensitivity, their practical application is often limited by high operational costs, time-consuming sample preparation, reliance on sophisticated instrumentation, and the need for trained personnel. In recent years, alternative methods such as enzyme-linked immunosorbent assays (ELISA)[16,17] and aptamer-based biosensors[18,19] have

[a]*Xiangya School of Public Health, Central South University, Changsha, Hunan, 410013, China. E-mail: pingshui@csu.edu.cn*
[b]*University of South China, Hengyang, Hunan, 421001, China*
[c]*Guangzhou Customs District, Guangzhou, Guangdong, 510470, China*
[d]*Department of Food Testing and Research, Hunan Testing Institute of Product and Commodity Supervision, Changsha, Hunan, 410007, China*
[e]*Intelligent Textile Institute of Innovation, Hunan Engineering University, Xiangtan, Hunan, 411104, China*
[f]*Hunan Provincial Key Laboratory of the Research and Development of Novel Pharmaceutical Preparations, Changsha Medical University, Provincial First-Class Applied Discipline (Pharmacy), Changsha, Hunan, 410219, China*
† Pian Wu and Jun Liu contributed equally to this work.

garnered attention for their rapid response and relatively simple operation. However, these approaches are hindered by the high cost of reagents and technical challenges associated with aptamer development and specificity.

Electrochemical sensing technology has emerged as a promising alternative due to its advantages of portability, automation, low cost, high sensitivity, and real-time detection capabilities.[20–22] The electrochemical oxidation of ENR occurs at the anode potential, facilitated by the ethyl group on the piperazine moiety, which enhances the susceptibility of the adjacent α-carbon to oxidation.[23,24] This oxidation process results in the formation of acetaldehyde as a by-product and generates ciprofloxacin.[25,26] ENR exhibits a characteristic oxidation potential approximately 0.9 V relative to the Ag/AgCl reference electrode. Nevertheless, direct detection of ENR using bare electrodes is often constrained by poor electron transfer efficiency and low sensitivity, underscoring the need for electrode surface modification to enhance signal transduction.

Covalent organic frameworks (COFs) have recently been recognized as a distinct class of crystalline porous materials, succeeding the development of inorganic porous materials and metal–organic frameworks (MOFs).[27,28] Constructed from light-element-based organic units interconnected by robust covalent bonds, COFs possess well-defined pore structures, high specific surface areas, and excellent thermal and chemical stability.[29,30] In contrast to amorphous polymers, which have irregular and poorly controlled pore distributions, COFs offer ordered nanochannels that facilitate molecular diffusion and charge transport, thereby enhancing the performance of electrochemical sensors through signal amplification and improved sensitivity.[31,32] However, a major limitation of COFs is their inherently low electrical conductivity, which restricts their direct application in electrochemical sensing.[33] To overcome this drawback, COFs are often combined with conductive materials to form hybrid composites. Reduced graphene oxide (RGO), owing to its large surface area, excellent electrical conductivity, and minimal oxygen-containing functional groups, has been extensively used in electrochemical applications.

In this work, a novel composite material, TAPB–PDA-COFs/RGO (TAPB: 3,5-tris(4-aminophenyl)benzene, PDA: *p*-phthalaldehyde), was synthesized by integrating TAPB–PDA-based COFs with RGO. The combination exploits π–π interactions between the conjugated structures of COFs and the carbon lattice of RGO to form a stable and conductive composite. The TAPB–PDA-COFs/RGO composite exhibited synergistic properties, including the well-defined pore architecture of COFs for efficient analyte diffusion and the excellent electrical conductivity of RGO for enhanced electron transfer, thereby improving the sensitivity and detection performance for ENR. This method not only enables rapid and efficient detection of ENR in aquatic environments but also provides a versatile platform for the development of electrochemical sensors targeting a broad range of fluoroquinolone antibiotics.

2 Experiments

2.1 Synthesis of TAPB–PDA-COFs/RGO composites

To prepare the TAPB–PDA-COFs/RGO composite, 10 mg of RGO was suspended in 5 mL of ultrapure water (final concentration: 2 mg mL^{-1}) and sonicated in the dark for 30 min to yield a uniform black suspension. Equal volumes of 2.0 mg mL^{-1} TAPB–PDA-COFs and 2.0 mg per mL RGO suspensions were then mixed at a 1 : 1 volume ratio and subjected to ultrasonication for an additional 30 min to form the composite. The mixture was subsequently centrifuged at 10 000 rpm for 5 min, and the precipitate was washed three times with ultrapure water. The final product was vacuum-dried overnight and stored at 4 °C in the dark until use.

2.2 Preparation of TAPB–PDA-COFs/RGO/GCE

The bare GCE was sequentially polished to a mirror-like finish using 1.0 μm, 0.3 μm, and 0.05 μm alumina slurry on a polishing cloth. The electrode was then ultrasonically cleaned in ethanol followed by ultrapure water to remove any residual polishing agents. After drying at room temperature, 4.0 μL of the TAPB–PDA-COFs/RGO dispersion was drop-cast onto the surface of the cleaned GCE and allowed to dry under dark conditions at ambient temperature. For comparison, TAPB–PDA-COFs/GCE and RGO/GCE were fabricated following the same protocol, substituting the composite suspension with dispersions of the respective individual materials.

Electrochemical analyses were performed using a CHI660E workstation configured in a standard three-electrode system, consisting of the modified GCE as the working electrode, an Ag/AgCl reference electrode (3.0 mol per L KCl), and a platinum wire counter electrode. Cyclic voltammetry (CV) was conducted at varying scan rates within a potential window of 0 to +1200 mV. Square wave voltammetry (SWV) measurements were carried out from +400 mV to +1200 mV with a pulse amplitude of 75 mV and a frequency of 20 Hz. All experiments were performed in 5 mL of ENR solution. Prior to each measurement, the working electrodes were incubated in the ENR standard solution for 43 s to facilitate sufficient analyte adsorption.

2.3 Conditional optimization: response surface methodology

Building on the results of single-factor optimization, a Box–Behnken Design (BBD) was utilized to refine the experimental parameters by investigating three variables at three levels. The selected independent variables included the modification volume of the composite material (*A*: X_1), the pH of the PBS solution (*B*: X_2), and the incubation time (*C*: X_3). The peak oxidation current (i_p) of ENR was used as the response variable. The design matrix, including 17 experimental runs, including five replicates at the center point to ensure model reliability, is presented in Table S1. The experimental data were modeled using a second-order polynomial equation as follows:

$$Y = \beta_0 + \sum \beta_i X_i + \sum \beta_{ii} X_{ii}^2 + \sum \beta_{ij} X_i X_j$$

where Y represents the predicted response (peak current), β_0 is the intercept, β_i, β_{ii}, and β_{ij} are the coefficients for the linear, quadratic, and interaction terms, respectively, and X_i and X_j are the coded levels of the independent variables.

Analysis of variance (ANOVA) was employed to assess the statistical significance of the model and its constituent terms. The significance of each regression coefficient and the interactions among variables was determined based on the associated *P*-values. All response surface methodology (RSM) analyses were conducted using Design-Expert software (version 8.0.6).

2.4 Detection of ENR in actual samples

To evaluate the practical applicability and reliability of the TAPB–PDA-COFs/RGO-based electrochemical sensor for ENR quantification in real samples, local tap water was employed as the test matrix. Samples were diluted with PBS and spiked with ENR (6 μmol L^{-1}, 18 μmol L^{-1}, and 54 μmol L^{-1}). Quantification was carried out using the standard addition method. For validation, the same spiked samples were analyzed by high-performance liquid chromatography (HPLC) following the Chinese national standard GB 29692-2013. Recovery rates from both techniques were calculated and compared to assess the accuracy and reliability of the electrochemical sensing platform.

3 Results and discussion

3.1 Working principle of the proposed electrochemical sensing platform

The electrochemical sensing platform based on TAPB–PDA-COFs/RGO was illustrated in Scheme 1. TAPB–PDA-COFs were synthesized using an ultrasonic method, followed by the formation of TAPB–PDA-COFs/RGO composites *via* ultrasonic blending of RGO and TAPB–PDA-COFs. The resulting TAPB–PDA-COFs/RGO composite was subsequently drop-cast onto GCE to fabricate the TAPB–PDA-COFs/GCE working electrode. Upon adsorption of ENR onto the TAPB–PDA-COFs, the peak current was measured using cyclic voltammetry (CV). The concentration of ENR was then quantified based on the observed changes in peak current.

3.2 Characterization of the composites

The morphologies of RGO and TAPB–PDA-COFs/RGO composites were analyzed using TEM. As illustrated in the Fig. 1A and B, RGO exhibited a wrinkled, thin-layered morphology, which indicated a high specific surface area. The presence of wrinkles is a typical structural feature of graphene.[34] Upon incorporating RGO into the thin-sheet structure of TAPB–PDA-COFs, the degree of wrinkling in the TAPB–PDA-COFs/RGO composite

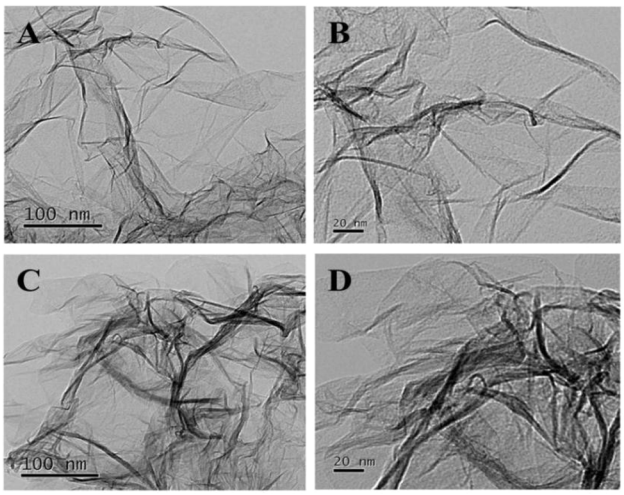

Fig. 1 SEM images of (A and B) RGO and (C and D) TAPB–PDA-COFs/RGO.

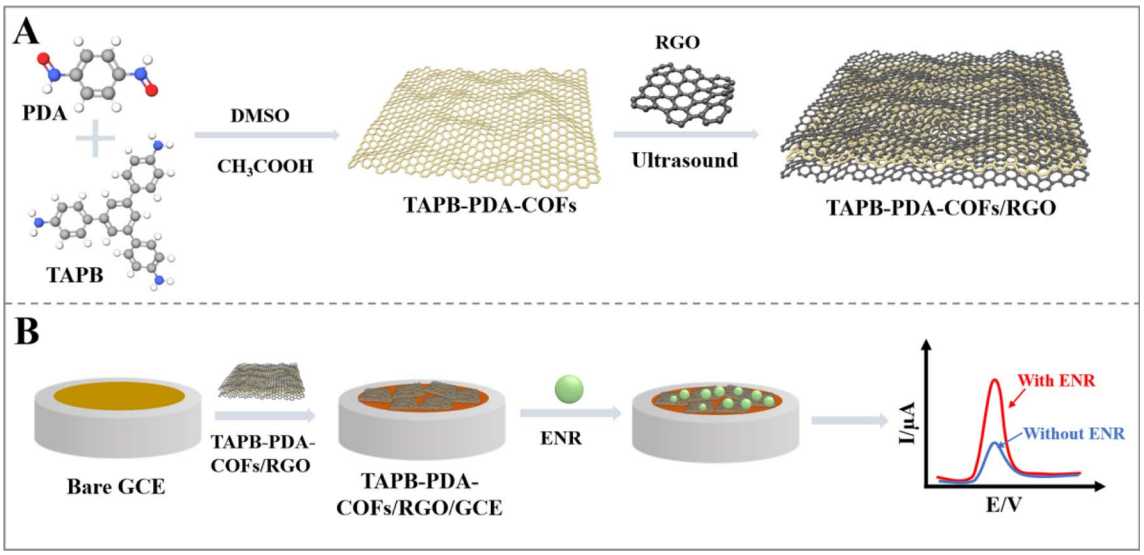

Scheme 1 Schematic diagram of (A) the preparation of TAPB–PDA-COFs/RGO composites, and (B) detection of ENR by an electrochemical sensing platform based on TAPB–PDA-COFs/RGO.

material increased (Fig. 1C and D). This resulted in a material with an expanded specific surface area, improved pore structure, and potentially enhanced conductivity.

To investigate the synthesis of TAPB–PDA-COFs/RGO composites, FTIR spectroscopy was employed to analyze GO, RGO, and TAPB–PDA-COFs/RGO composites, with the aim of identifying relevant functional groups and examining the synthesis process and structural characteristics of the composites (Fig. 2A and B). The FTIR spectrum of GO revealed several characteristic functional groups, including aromatic C–C bonds at 1620 cm^{-1}, epoxy C–O groups at 1250 cm^{-1}, carbonyl C═O groups at 1725 cm^{-1}, carboxyl O═C–O groups at 1400 cm^{-1}, and alkoxy C–O groups at 1066 cm^{-1}. The broad absorption band at 3410 cm^{-1} corresponded to the stretching vibration of hydroxyl (–OH) groups. Upon reduction to RGO, the peaks at 1725 cm^{-1}, 1400 cm^{-1}, and 1066 cm^{-1} disappeared, while the C–O bond (associated with epoxy or alkoxy groups) remained at 1237 cm^{-1}. In the spectrum of TAPB–PDA-COFs, the characteristic C═N peak appeared at 1622 cm^{-1}, and a peak at 821 cm^{-1} was attributed to the skeletal vibration of the C–C bond. The FTIR spectrum of the TAPB–PDA-COFs/RGO composite closely resembled that of RGO, but a new peak appeared at 821 cm^{-1}, consistent with the skeletal vibration of C–C in TAPB–PDA-COFs, indicating the successful fabrication of the composite. To further analyze the crystal structure of the materials, XRD patterns were obtained for GO, RGO, TAPB–PDA-COFs, and TAPB–PDA-COFs/RGO composites (Fig. S1). The XRD pattern of GO revealed a strong peak at 11.49° and a weaker

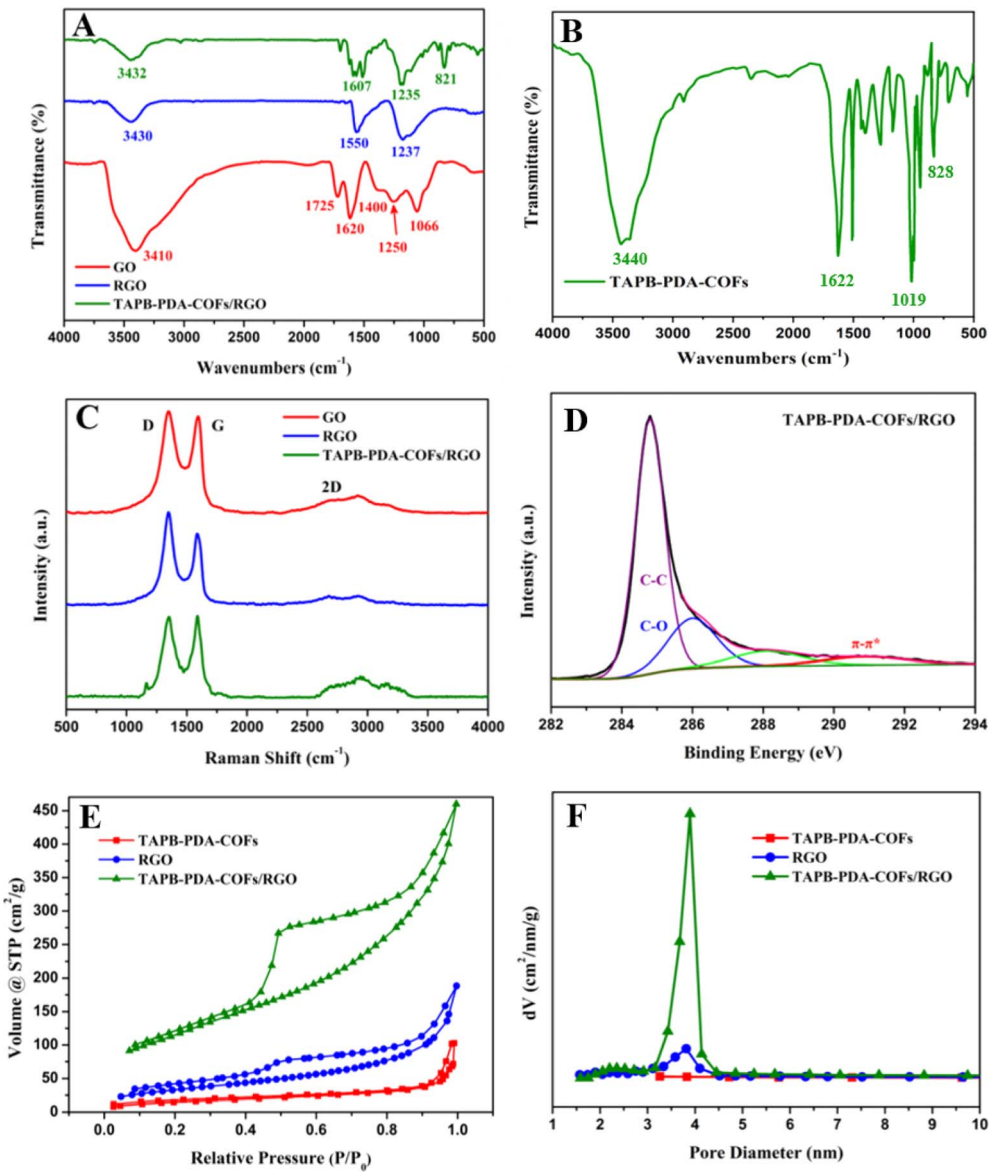

Fig. 2 (A) FTIR of GO, RGO and TAPB–PDA-COFs/RGO. (B) FTIR of TAPB–PDA-COFs. (C) Raman of GO, RGO and TAPB–PDA-COFs/RGO. (D) C 1s XPS analysis of TAPB–PDA-COFs/RGO. (E) N_2 adsorption–desorption isotherm of RGO, TAPB–PDA-COFs, and TAPB–PDA-COFs/RGO. (F) The pore size distribution of RGO, TAPB–PDA-COFs, and TAPB–PDA-COFs/RGO.

peak at 43.02°, corresponding to the (001) and (100) crystal planes, respectively.[35] After reduction, the RGO pattern showed a new peak at 23.01°, corresponding to the (002) crystal plane, while the peak at 11.49° disappeared. The XRD pattern of the TAPB–PDA-COFs/RGO composite closely resembles that of RGO, suggesting that the incorporation of COFs did not significantly alter the crystalline structure of RGO.

Moreover, Raman spectroscopy of GO, RGO, and TAPB–PDA-COFs/RGO composites was performed using 532 nm excitation light to investigate the carbon network and 2D structures of the materials (Fig. 2C). The D peak and G peak of GO and RGO were observed at 1348 cm^{-1} and 1594 cm^{-1}, respectively, which aligned with existing literature.[36] The D peak corresponded to defects within the carbon structure, whereas the G peak was characteristic of sp^2 hybridized carbon networks.[37] Both the RGO and TAPB–PDA-COFs/RGO spectra showed a slight reduction in the intensity of these peaks compared to GO, a result of the removal of oxygen-containing functional groups in RGO and the partial restoration of the graphite structure. The G peak intensity of TAPB–PDA-COFs/RGO is higher than that of RGO, suggesting an increase in the sp^2 hybridized carbon network, which indicated the successful incorporation of COFs into the composite.[37] The D-to-G peak intensity ratio in the TAPB–PDA-COFs/RGO composite declined from 1.20 in RGO to 1.01, signifying that defects in the material have been partially repaired and the aromatic structure of graphene has been partially restored. Additionally, the 2D peak, observed at 2701 cm^{-1} in the Raman spectrum of TAPB–PDA-COFs/RGO, further confirmed the presence of a multilayer structure in the synthesized composite.

Building upon the previous analyses, XPS was utilized to investigate the chemical states of the TAPB–PDA-COFs/RGO composite and to elucidate the principles underlying its synthesis. The C 1s peak of TAPB–PDA-COFs/RGO was deconvoluted into three distinct peaks at binding energies of 284.8 eV, 286 eV, and 287.98 eV, attributed to C–C, C–O, and C═O bonds, respectively (Fig. 2D).[38] Similarly, the C 1s peak of RGO, upon separation, also displayed three peaks at 284.8 eV, 286 eV, and 288.1 eV, confirming that the binding energies for C–C, C–O, and C═O in RGO align closely with those observed in TAPB–PDA-COFs/RGO (Fig. S2A). In contrast, the C 1s peak of TAPB–PDA-COFs was resolved into two peaks at 284.8 eV and 285.9 eV, attributed to the C–C and C–O binding energies, respectively. The highest peak intensities at C–C and C–O for the composite further support the successful synthesis of TAPB–PDA-COFs/RGO. Additionally, a weak peak near 291 eV was observed in the spectra of all three materials, which is attributed to the π–π* vibrational satellite peak.[37] Notably, the peak intensity correlates with the presence of phenyl groups, with the TAPB–PDA-COFs/RGO composite displaying the highest intensity, thereby confirming π–π conjugation between RGO and TAPB–PDA-COFs within the composite.

The specific surface area and pore size of RGO, TAPB–PDA-COFs, and their composite were evaluated *via* N_2 adsorption–desorption isotherms at 77 K. As illustrated in Fig. 2E, RGO exhibited a substantially larger pore volume (0.6943 $cm^3\ g^{-1}$) and BET surface area (404.1 $m^2\ g^{-1}$). TAPB–PDA-COFs showed a pore volume of 0.1589 $cm^3\ g^{-1}$ and a BET surface area of 54.91 $m^2\ g^{-1}$, whereas the TAPB–PDA-COFs/RGO composite presented intermediate values of 0.2968 $cm^3\ g^{-1}$ and 142 $m^2\ g^{-1}$, respectively. The enhanced surface area of the composite, primarily attributed to the high specific surface area of RGO, promoted the accumulation of ENR during detection. Furthermore, the average pore size of RGO was 6.762 nm, while that of TAPB–PDA-COFs was 3.195 nm. In the TAPB–PDA-COFs/RGO composite, the average pore size increased to 9.612 nm (Fig. 2F). This enlargement of the pore size enhances the material's ability to facilitate electron transfer during electrochemical reactions, thus improving the sensitivity of ENR detection.

TGA was conducted to assess the thermal stability of RGO, TAPB–PDA-COFs, and TAPB–PDA-COFs/RGO (Fig. S3). The TGA results indicated that all three materials exhibited significant mass loss at temperatures above 400 °C. However, the TAPB–PDA-COFs/RGO composite demonstrated the lowest mass loss below 400 °C. This enhanced stability is attributed to the relatively higher stability of RGO. Consequently, when combined with TAPB–PDA-COFs, the TAPB–PDA-COFs/RGO composite exhibits superior stability, making it more advantageous for applications requiring thermal resilience.

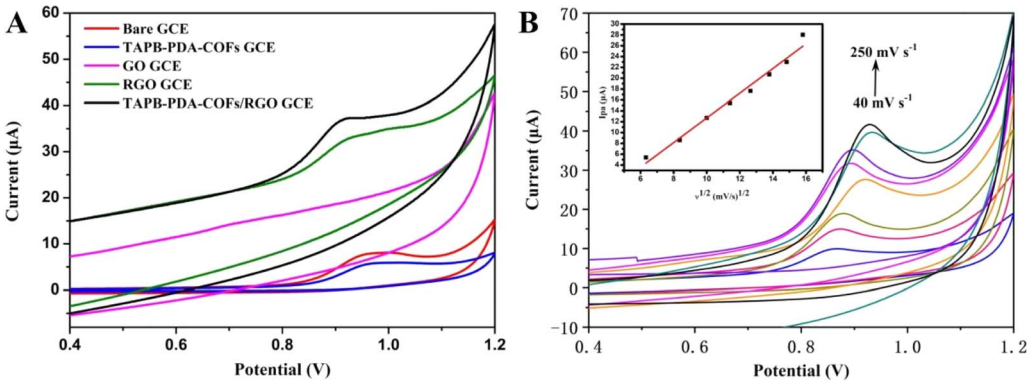

Fig. 3 (A) CV characterization of different modified electrodes with ENR. (B) CV image of TAPB–PDA-COFs/RGO/GCE at different scan rates. The inset is a linear graph of redox peak current and the square root of the scan rate.

3.3 Feasibility verification of the proposed electrochemical sensing platform

To assess the current enhancement achieved by the TAPB–PDA-COFs/RGO modified GCE electrode, a comparative experiment was conducted, wherein the peak currents of various modified electrodes were compared at the same concentration of ENR. As illustrated in Fig. 3A and S4, the TAPB–PDA-COFs/RGO/GCE electrode produced the highest peak current, demonstrating superior electron-transfer capability of the TAPB–PDA-COFs/RGO composite. This improvement can be ascribed to the synergistic integration of the large specific surface area and high porosity of TAPB–PDA-COFs with the excellent electrical conductivity of RGO. Moreover, the extended π-conjugated structures of both TAPB–PDA-COFs and RGO facilitate strong π–π stacking interactions with the aromatic quinoline and benzene rings of ENR molecules. In addition, hydrogen bonding may occur between the imine (C=N) linkages of the COF framework and the carboxyl (–COOH), carbonyl (C=O), and fluorine (–F) functional groups of ENR, further enhancing the adsorption and preconcentration of ENR at the electrode surface. Furthermore, CV measurements at different scan rates showed a distinct increase in anodic peak current (i_p) with increasing scan rate (ν) (Fig. 3B). The inset of Fig. 3B further showed a strong linear correlation between the peak current and the square root of the scan rate ($\nu^{1/2}$). The linear regression equation was $i_p\ (\mu A) = -10.0299 + 2.2725\nu^{1/2}\ (\mathrm{mV\ s^{-1}})^{1/2}$ ($R^2 = 0.977$). These findings indicated that the electrochemical reaction of ENR on the TAPB–PDA-COFs/RGO/GCE was diffusion-controlled, confirming its suitability for ENR detection.

3.4 Optimization of experimental conditions

The conductivity of the TAPB–PDA-COFs/RGO composite is significantly influenced by the ratio of RGO to TAPB–PDA-COFs, which in turn affects the peak current generated during the electrochemical detection of ENR. To optimize the performance of the TAPB–PDA-COFs/RGO composite, the concentration of TAPB–PDA-COFs in the TAPB–PDA-COFs/RGO composite was evaluated. As shown in Fig. S5A, an increase in the concentration of TAPB–PDA-COFs solution lead to a rapid enhancement in the peak current for ENR detection. The peak current reaches its maximum value when the concentration of TAPB–PDA-COFs solution was 1.0 mg mL^{-1}. However, further increased in the concentration of TAPB–PDA-COFs result in a significant decline in peak current. This behavior can be ascribed to the highly ordered porous architecture of the TAPB–PDA-COFs, which offers an extensive and accessible surface area conducive to the enrichment of ENR molecules. Such structural characteristics facilitate analyte accumulation near the electrode interface and effectively shorten the diffusion pathway, thereby enhancing electrochemical response. However, when the concentration of TAPB–PDA-COFs becomes excessively high, the insulating nature of the COF framework begins to impede the intrinsic conductivity of RGO, resulting in a diminished current signal. To achieve an optimal balance between electrical conductivity and the structural advantages provided by the COF's porosity and active sites, a TAPB–PDA-COF concentration of 1.0 mg mL^{-1} was selected for subsequent experiments. Subsequently, the detection system conditions were optimized. The results from the single-factor experimental optimization indicated the optimal parameters were determined as follows: a modification volume of 4 μL for the TAPB–PDA-COFs/RGO composite, a PBS buffer pH of 7, and an incubation time of 80 s for the TAPB–PDA-COFs/RGO/GCE electrode (Fig. S5B–D).

To further assess potential interactions between these factors, the response surface methodology was employed for additional optimization after the single-factor conditions were established. Total 17 runs were carried out according to the Box–Behnken design (Table S2). The peak current ranged from 12.70 μA to 21.38 μA. The final equations between tested factors and response were presented as following:

$$Y = -239.8298 + 4.5485A + 64.277B + 0.60945C + 0.16875AB - 0.02819AC - 0.013625BC - 0.41731A^2 - 4.67925B^2 - 0.0037C^2$$

The results of the variance analysis for the response surface quadratic model were presented in Table S3. The model exhibited an F-value of 22.28 with a corresponding P-value below 0.05, indicating that the model was significant. The R^2 is 0.9663, suggesting the good correlation between the predicted and observed values. Furthermore, the lack-of-fit test yielded an F-value of 1.86 and a P-value greater than 0.05, indicating that the lack of fit is not statistically significant. The model also demonstrated an adequate signal-to-noise ratio of 11.508, suggesting that the signal was sufficient for reliable interpretation and predictive analysis.

The 3D response surface plot visually illustrates the interactions among the independent variables on the current response (Fig. 4). In this model, composite modified volume (A), pH (B), and incubation time (C) were not significant. The quadratic terms (A^2, B^2, and C^2) exhibited P-values less than 0.05, suggesting that their effects were significant. Among the interaction terms, AB and BC were not significant ($P > 0.05$), whereas AC was significant ($P < 0.05$). This indicated a synergistic effect between the composite material modification volume and the incubation time, which jointly influence the peak current response. Based on BBD analysis and practical application considerations, the optimal experimental conditions for ENR detection were determined as follows: composite material modification volume of 4.0 μL, pH of 7.0, and incubation time of 78 s.

To validate the predictive accuracy of the model, three replicate experiments were conducted under these optimized conditions. The average peak current obtained was 20.39 μA, closely aligning with the model's predicted value. This result confirmed the reliability of the model and the suitability of the optimized conditions for practical application.

3.5 Detection performance of ENR

Following established experimental procedures, a TAPB–PDA-COFs/RGO-based electrochemical sensing platform was employed for the detection of various concentrations of ENR.

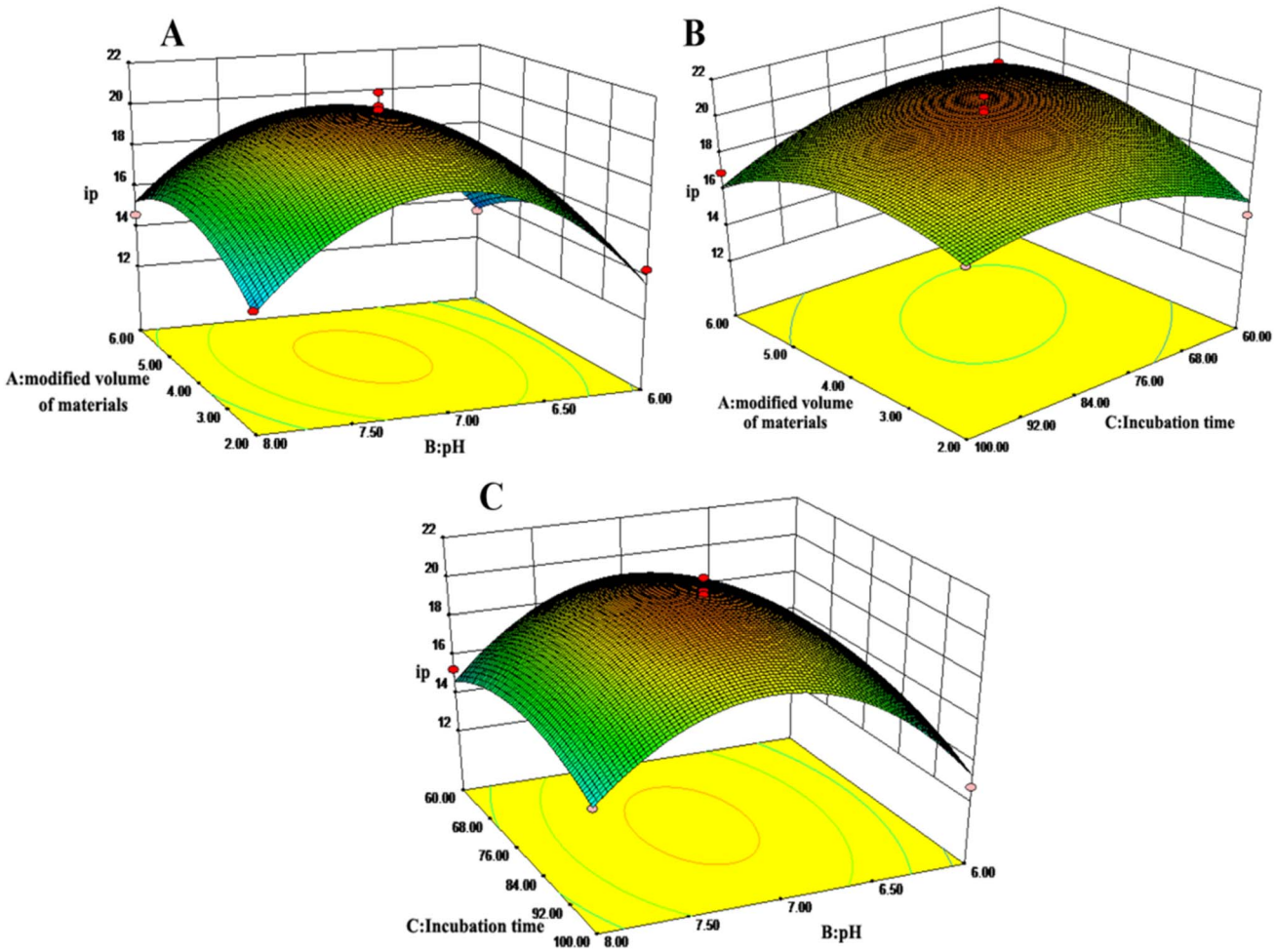

Fig. 4 Response surface for the effects on i_p. (A) Response surface plot for modified volume of the materials and pH. (B) Response surface plot for modified volume of the materials and incubation time. (C) Response surface plot for pH and incubation time.

The square wave voltammetry (SWV) responsed corresponding to varying ENR were illustrated in Fig. 5A. The peak current exhibited a positive correlation with ENR concentration, showing a gradual increase within the concentration range of 0.01 μmol L^{-1} to 150 μmol L^{-1}. Two calibration curves were established by plotting the peak current *versus* ENR concentration (Fig. 5B). The corresponding linear regression equations were: $y = 0.504x + 0.6047$ for the range of 0.01–8.0 μmol L^{-1} ($R^2 = 0.9913$), and $y = 5.1519x + 0.1293$ for the range of 8.0–150 μmol L^{-1} ($R^2 = 0.984$), respectively. The limit of detection (LOD) calculated as $3S/K$ (S was the standard deviation of 11 blank measurements and K was the slope of the calibration curve), was determined to be 0.028 μmol L^{-1}. Compared to previously reported methods, the TAPB–PDA-COFs/RGO-based electrochemical sensing platform demonstrated an extended linear range and enhanced sensitivity for ENR detection (Table 1).

Interference resistance is a critical parameter for assessing the performance of the TAPB–PDA-COFs/RGO-based electrochemical sensing platform. To assess the anti-interference capability, equal concentrations (8 μmol L^{-1} and 100 μmol L^{-1}) of ENR, ofloxacin, norfloxacin, ciprofloxacin, and a combined solution of all four antibiotics (denoted as Mix) were tested. As shown in Fig. 5C, the sensor exhibited the highest peak currents for ENR and the mixture, with values that were closely aligned. In contrast, the peak currents for ciprofloxacin, norfloxacin, and ofloxacin were significantly lower. These results demonstrated that the sensor possessed high selectivity for ENR, even in the presence of structurally similar fluoroquinolone antibiotics, indicating strong anti-interference performance. The preferential response to ENR suggested a specific interaction or molecular affinity between the TAPB–PDA-COFs/RGO composite and ENR molecules. This selective binding likely enhances the efficiency of electron transfer during detection, thereby enabling accurate and reliable quantification of ENR. However, while the present study primarily focused on selectivity toward structurally related fluoroquinolones, future work should systematically evaluate the impact of natural organic matter to provide a more comprehensive assessment of the sensor's anti-interference performance in realistic environmental water matrices.

In addition, the stability of the electrode modification method was systematically evaluated. TAPB–PDA-COFs/AuNPs/GCE electrodes were fabricated under identical conditions for the detection of ENR and stored at 4 °C. The peak current on the first day was used as a reference to calculate the relative current

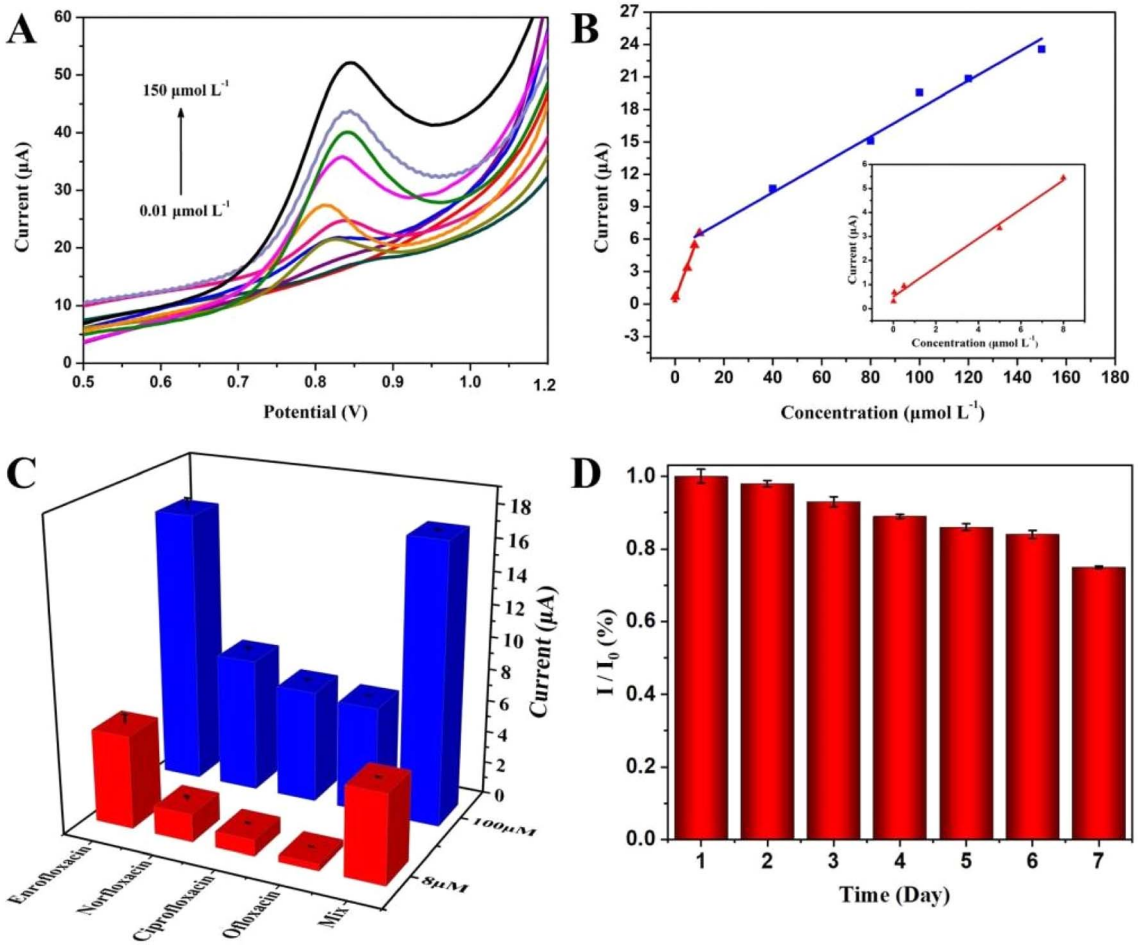

Fig. 5 (A) SWV characterization of a range of concentrations for ENR on the TAPB–PDA-COFs/RGO/GCE in PBS. (B) Calibration curve between ENR concentration and current response. The inset is an enlarged view of the calibration curve of the concentration range between 0.01 to 8 μmol L^{-1} ($n = 3$). (C) SWV current responses of TAPB–PDA-COFs/RGO-based sensor in ENR, ciprofloxacin, norfloxacin, ofloxacin, and mixture ($n = 3$). (D) The stability of TAPB–PDA-COFs/RGO-based electrochemical sensing platform ($n = 3$).

Table 1 Comparison of TAPB–PDA-COFs/RGO-based electrochemical sensing platform with other methods for ENR analysis

Materials	Signal	Linear range (μmol L^{-1})	LOD (μmol L^{-1})	Ref.
Bare GCE	Electrochemical	30.0–300.0	31.0 ± 4.6	39
CdS@ENR-TPB/CWE	Electrochemical	0.1–10000	0.095	40
AuNPs/MWCNT/PDDA-SGGT	Electrochemical	0.3–30.0	0.01	41
CoCH-6 h/GCE	Electrochemical	0.5–65.0	0.1	42
CeO_2NHR/GCE	Electrochemical	2.78–33.83	0.01	43
TAPB–PDA-COFs/AuNPs/GCE	Electrochemical	0.05–10.0 10.0–120.0	0.041	24
TAPB–PDA-COFs/RGO/GCE	Electrochemical	0.01–8.0 8.0–150.0	0.028	This work

responses over a 7 day period. As shown in Fig. 5D, the modified electrodes retained 89% of their initial response within the first three days. A gradual decline in current was observed from the fourth day onward, with the electrodes maintaining 84% of the original signal by the sixth day. On the seventh day, the current response decreased more markedly to 75%, indicating that the modified electrodes exhibit good short-term stability under refrigerated storage conditions.

3.6 Detection of real samples

The practical applicability of the TAPB–PDA-COFs/RGO-based electrochemical sensing platform was evaluated through the detection of ENR in tap water samples. These samples were

Table 2 Determination of ENR in real samples ($n = 3$)

		Developed sensing platform			HPLC		
Sample	Added (μmol L^{-1})	Detected (μmol L^{-1})	Recovery (%)	RSD (%)	Detected (μmol L^{-1})	Recovery (%)	RSD (%)
Water sample	0	ND[a]	—	—	ND[a]	—	—
	6	5.83 ± 0.52	97.1	8.9	ND[a]	—	—
	18	15.14 ± 1.27	84.1	8.4	14.9 ± 1.34	82.7	9.0
	54	53.81 ± 4.49	99.7	8.3	57.23 ± 4.43	102.2	7.7

[a] Not detected.

spiked with three concentrations of ENR (6 μmol L^{-1}, 18 μmol L^{-1}, and 54 μmol L^{-1}). As presented in Table 2, the TAPB–PDA-COFs/RGO-based electrochemical sensing platform achieved recoveries ranging from 84.1% to 99.7%, with relative standard deviations (RSDs) between 8.3% and 8.9%, demonstrating satisfactory accuracy and reproducibility. In comparison, the HPLC method yielded recoveries between 82.7% and 102.2%, with RSDs ranging from 7.7% to 9.0%. Notably, the HPLC method was unable to detect ENR at the lowest tested concentration (6 μmol L^{-1}), whereas the electrochemical sensor successfully quantified ENR at this level. These results demonstrated that the proposed electrochemical sensing platform not only provided comparable or superior recovery rates relative to the standard HPLC method but also offered advantages in terms of operational simplicity, reduced analysis time, and enhanced sensitivity for low-concentration ENR detection. Therefore, the sensor shows significant potential for practical application in environmental monitoring of antibiotic residues.

4 Conclusion

This work successfully developed a TAPB–PDA-COFs/RGO-based electrochemical sensing platform for the efficient detection of ENR in water samples. The composite material synthesized by integrating COF with RGO exhibited excellent structural and electrochemical characteristics, including increased surface area and improved analyte accessibility. The sensor demonstrated a broad linear detection range, a low detection limit, strong selectivity against interfering antibiotics, and good stability over time. Moreover, when applied to real tap water samples, the sensor provided accurate and reproducible results with recoveries comparable to or exceeding those of HPLC method, particularly at low ENR concentrations. Overall, the proposed platform offers a simple, cost-effective, and highly sensitive alternative for the monitoring of fluoroquinolone antibiotics in environmental settings, showing great promise for practical applications in environmental analysis and public health protection.

Conflicts of interest

The authors declare that they have no known competing financial interests or personal relationships that could have appeared to influence the work reported in this paper.

Data availability

The data supporting this article have been included as part of the supplementary information (SI). Supplementary information is available. See DOI: **https://doi.org/10.1039/d5ra07733h**.

Acknowledgements

This work was supported by the Science and Technology Plan of Hunan Provincial Administration for Market Regulation (Grant No. 2023KJH16), the Natural Science Foundation of Changsha (Grant No. kq2402240), the Natural Science Foundation of Hunan (No. 2025JJ60624), the National Natural Science Foundation of China (Grant No. 82373635), the Development Program of Hunan Province (No. 2024JK2159).

References

1 A. Abbas, A. Barkhouse, D. Hackenberger and G. D. Wright, Antibiotic resistance: a key microbial survival mechanism that threatens public health, *Cell Host Microbe*, 2024, **32**(6), 837–851.
2 M. I. Hutchings, A. W. Truman and B. Wilkinson, Antibiotics: past, present and future, *Curr. Opin. Microbiol.*, 2019, **51**, 72–80.
3 K. Kümmerer, Significance of antibiotics in the environment, *J. Antimicrob. Chemother.*, 2003, **52**(1), 5–7.
4 P. Barathe, K. Kaur, S. Reddy, V. Shriram and V. Kumar, Antibiotic pollution and associated antimicrobial resistance in the environment, *J. Hazard. Mater. Lett.*, 2024, **5**, 100105.
5 W. Yang, J. Li, Z. Yao and M. Li, A review on the alternatives to antibiotics and the treatment of antibiotic pollution: current development and future prospects, *Sci. Total Environ.*, 2024, **926**, 171757.
6 A. S. Maris, P. Mody, D. J. Brewer and R. M. Humphries, The Fluoroquinolones: an update for the clinical microbiologist, *Clin. Microbiol. Newsl.*, 2021, **43**(12), 97–107.
7 Y. Zhang, B. Duan, Q. Bao, T. Yang, T. Wei, J. Wang, C. Mao, C. Zhang and M. Yang, Aptamer-modified sensitive nanobiosensors for the specific detection of antibiotics, *J. Mater. Chem. B*, 2020, **8**(37), 8607–8613.
8 M. Abolhassani, M. Derafshi, A. Hassani and M. A. Delavar, Impacts of the application of enrofloxacin-containing

poultry manure on the soil microbial activities, *Environ. Processes*, 2023, **10**(2), 30.

9 A. Rico, M. R. Dimitrov, R. P. A. Van Wijngaarden, K. Satapornvanit, H. Smidt and P. J. Van den Brink, Effects of the antibiotic enrofloxacin on the ecology of tropical eutrophic freshwater microcosms, *Aquat. Toxicol.*, 2014, **147**, 92–104.

10 C. Wang, X. Y. Zhao, H. L. Zhang, H. Y. Wang and L. Sun, Comparative analysis on maximum residue limits for veterinary drugs in animal-derived food between China and codex alimentarius commission standards, *J. Food Saf. Food Qual.*, 2020, **11**, 7164–7169.

11 L. A. Cox Jr, Enrofloxacin in Poultry and Human Health, *Emerg. Infect. Dis.*, 2006, **12**, 872–873.

12 J. Dai, Y. Wang, H. Lin, Y. Sun, Y. Pan, J. Q. Qiao, H. Z. Lian and C. X. Xu, Residue screening and analysis of enrofloxacin and its metabolites in real aquatic products based on ultrahigh-performance liquid chromatography coupled with high resolution mass spectrometry, *Food Chem.*, 2023, **404**, 134757.

13 M. Pang, J. Xu, Y. Tang, Y. Guo, H. Ding, R. Wang, T. Zhang, G. Zhang, X. Guo, G. Dai, X. Xie and K. Xie, Combining GC-MS/MS with a LLE-SPE sample pretreatment step to simultaneously analyse enrofloxacin and ofloxacin residues in chicken tissues and pork, *Food Chem.*, 2024, **456**, 139972.

14 A. Junza, S. Barbosa, M. R. Codony, A. Jubert, J. Barbosa and D. Barrón, Identification of metabolites and thermal transformation products of quinolones in raw cow's milk by liquid chromatography coupled to high-resolution mass spectrometry, *J. Agric. Food Chem.*, 2014, **62**(8), 2008–2021.

15 D. Barrón, E. Jiménez-Lozano, J. Cano and J. Barbosa, Determination of residues of enrofloxacin and its metabolite ciprofloxacin in biological materials by capillary electrophoresis, *J. Chromatogr. B:Biomed. Sci. Appl.*, 2001, **759**(1), 73–79.

16 G. Hu, Z. Liu, Y. Zhang, K. He, S. Gao and J. Hao, Fluorescence quenching biomimetic ELISA based on quantum dots for enrofloxacin detection in animal-derived foods, *Microchem. J.*, 2024, **201**, 110589.

17 G. Hu, Z. Liu, Y. Zhang, S. Gao and J. Hao, Simultaneous detection of enrofloxacin and florfenicol in animal-derived foods based on fluorescence quenching BELISA and a nanozyme catalytic strategy, *Talanta*, 2024, **280**, 126759.

18 T. Mathai, T. Pal, N. Prakash and S. Mukherji, Portable biosensor for the detection of Enrofloxacin and Ciprofloxacin antibiotic residues in food, body fluids, environmental and wastewater samples, *Biosens. Bioelectron.*, 2023, **237**, 115478.

19 S. Y. Lam, P. Li, L. Jin, H. Y. Chan, Y. Ruan, C. K. Kwok and P. K. Lo, Enhanced detection of enrofloxacin in seawater using a newly selected aptamer on a graphite oxide-based biosensor, *Anal. Chem.*, 2025, **97**(12), 6735–6744.

20 V. A. T. Ezhil, P. Puthiaraj, C. H. Kwak, S. K. Choe, Y. S. Huh, W. S. Ahn and Y. K. Han, Electrochemical determination of quercetin based on porous aromatic frameworks supported Au nanoparticles, *Electrochim. Acta*, 2016, **216**, 181–187.

21 A. T. Ezhil Vilian, R. Sivakumar, Y. S. Huh, J. H. Youk and Y. K. Han, Palladium supported on an amphiphilic triazine–urea-functionalized porous organic polymer as a highly efficient electrocatalyst for electrochemical sensing of rutin in human plasma, *ACS Appl. Mater. Interfaces*, 2018, **10**(23), 19554–19563.

22 V. A. T. Ezhil, J. N. Tiwari, M. Alhammadi, G. Bhaskaran, S. K. Hwang, S. Kim, K. Kumar, A. S. Kumar, Y. S. Huh and Y. K. Han, Palladium nanoparticles anchored MoS_2-MXene composite modified electrode for rapid sensing of toxic bisphenol A in aqueous media, *Chem. Eng. J.*, 2023, **469**, 144017.

23 N. Karuppusamy, V. Mariyappan, S. M. Chen and R. Ramachandran, A novel electrochemical sensor for the detection of enrofloxacin based on a 3D flower-like metal tungstate-incorporated reduced graphene oxide nanocomposite, *Nanoscale*, 2022, **14**(4), 1250–1263.

24 S. Lu, S. Wang, P. Wu, D. Wang, J. Yi, L. Li, P. Ding and H. Pan, A composite prepared from covalent organic framework and gold nanoparticles for the electrochemical determination of enrofloxacin, *Adv. Powder Technol.*, 2021, **32**(6), 2106–2115.

25 M. Antilén, C. Valencia, E. Peralta, C. Canales, C. Espinosa-Bustos and M. Escudey, Enrofloxacin behavior in presence of soil extracted organic matter: an electrochemical approach, *Electrochim. Acta*, 2017, **244**, 104–111.

26 J. Liu, H. Tang, B. Zhang, X. Deng, F. Zhao, P. Zuo, B. C. Ye and Y. Li, Electrochemical sensor based on molecularly imprinted polymer for sensitive and selective determination of metronidazole via two different approaches, *Anal. Bioanal. Chem.*, 2016, **408**(16), 4287–4295.

27 K. T. Tan, S. Ghosh, Z. Wang, F. Wen, D. Rodríguez-San-Miguel, J. Feng, N. Huang, W. Wang, F. Zamora, X. Feng, A. Thomas and D. Jiang, Covalent organic frameworks, *Nat. Rev. Methods Primers*, 2023, **3**(1), 1.

28 Y. Li, W. Chen, G. Xing, D. Jiang and L. Chen, New synthetic strategies toward covalent organic frameworks, *Chem. Soc. Rev.*, 2020, **49**(10), 2852–2868.

29 M. S. Lohse and T. Bein, Covalent organic frameworks: structures, synthesis, and applications, *Adv. Funct. Mater.*, 2018, **28**(33), 1705553.

30 K. Geng, T. He, R. Liu, S. Dalapati, K. T. Tan, Z. Li, S. Tao, Y. Gong, Q. Jiang and D. Jiang, Covalent organic frameworks: design, synthesis, and functions, *Chem. Rev.*, 2020, **120**(16), 8814–8933.

31 R. Xue, Y. S. Liu, S. L. Huang and G. Y. Yang, Recent progress of covalent organic frameworks applied in electrochemical sensors, *ACS Sens.*, 2023, **8**(6), 2124–2148.

32 Z. Meng and K. A. Mirica, Covalent organic frameworks as multifunctional materials for chemical detection, *Chem. Soc. Rev.*, 2021, **50**(24), 13498–13558.

33 S. Bommakanti, I. Mondal, B. R. Sahu, S. Nath, S. P. Senanayak and B. P. Biswal, Functionality-dependent electrical conductivity in two-dimensional covalent organic fFrameworks, *J. Phys. Chem. C*, 2023, **127**(17), 8352–8361.

34 Z. Yu, C. Xiao, Y. Huang, M. Chen, W. Wei, X. Yang, H. Zhou, X. Bi, L. Lu, J. Ruan and X. Fan, Enhanced bioactivity and

osteoinductivity of carboxymethyl chitosan/nanohydroxyapatite/graphene oxide nanocomposites, *RSC Adv.*, 2018, **8**(32), 17860–17877.

35 Z. Jiang, W. Chen, L. Jin, F. Cui, Z. Song and C. Zhu, High performance acetylene sensor with heterostructure based on WO_3 nanolamellae/reduced graphene oxide (rGO) Nanosheets operating at low temperature, *Nanomaterials*, 2018, **8**(11), 909.

36 P. M. L. F. Pompeu, E. Buffon and N. R. Stradiotto, Electrochemical sensor based on reduced graphene oxide and molecularly imprinted poly(phenol) for d-xylose determination, *Talanta*, 2020, **208**, 120379.

37 S. Nuthalapati, V. Shirhatti, V. Kedambaimoole, N. Neella, M. M. Nayak, K. Rajanna and H. Takao, Highly sensitive, scalable reduced graphene oxide with palladium nanocomposite as strain sensor, *Nanotechnology*, 2020, **31**(3), 035501.

38 Y. Hong, Y. Li, F. Wang, B. Zuo, X. Wang, L. Zhang, D. Kawaguchi and K. Tanaka, Enhanced thermal stability of polystyrene by interfacial noncovalent interactions, *Macromolecules*, 2018, **51**(15), 5620–5627.

39 C. Canales, E. Peralta and M. Antilen, Electrochemical techniques to detect and quantify Enrofloxacin in presence of highly potential interferences: assays in Chilean aqueous-soil matrices, *J. Electroanal. Chem.*, 2019, **832**, 329–335.

40 L. A. O. Yuting, Z. Jing and L. Donghui, Preparation of cadmium sulfide nanoparticles and their application for improving the properties of the electrochemical sensor for the determination of enrofloxacin in real samples, *Chirality*, 2019, **31**(3), 174–184.

41 Y. Cao, H. Qu, B. Dong, Y. Mao and L. Zheng, Highly sensitive and selective detection of enrofloxacin residues in chicken based on solution-gated graphene field-effect transistors, *J. Electroanal. Chem. Interfacial Electrochem.*, 2023, **935**, 117325.

42 Q. Yu, H. Yang and Y. Yang, Fabrication of an electrochemical sensor for the rapid and sensitive detection of enrofloxacin in meat samples, *J. Food Meas. Char.*, 2024, **18**(1), 87–94.

43 A. Chakravorty and V. Raghavan, Fabrication of sensors with microwave-assisted porous CeO_2 nanohorns based on electrochemical oxidation of enrofloxacin and ciprofloxacin-Fostering one health for sustainable future, *Microchem. J.*, 2025, **213**, 113710.